Rare Metal Materials and Engineering
Volume 50, Issue 3, March 2021
Available online at www.rmme.ac.cn

Science Press

Cite this article as: Rare Metal Materials and Engineering, 2021, 50(3): 0853-0859.

ARTICLE

Effect of Tantalum Content on Mechanical and Corrosion Behavior of Ti-6Al-3Nb-2Zr-1Mo-*x*Ta Alloys

Wang Qi[1,3], Ren Junqiang[2], Zhang Binbin[3], Wu Yukun[3], Ye Miao[1], Shao Shan[2]

[1] Huanghuai University, Zhumadian 463000, China; [2] State Key Laboratory of Advanced Processing and Recycling of Nonferrous Metals, Department of Materials Science and Engineering, Lanzhou University of Technology, Lanzhou 730050, China, [3] Luoyang Ship Materials Research Institute, Luoyang 471039, China

Abstract: The microstructure, tensile properties, Charpy impact toughness and corrosion resistance of Ti-6Al-3Nb-2Zr-1Mo-*x*Ta (x=0, 0.2, 0.5, 1.0, 3.0, 5.0) alloys were investigated. The results indicate that except Ti-6Al-3Nb-2Zr-1Mo-5Ta alloy with lamellar structure, the bimodal structure is observed in Ti-6Al-3Nb-2Zr-1Mo-*x*Ta (x=0, 0.2, 0.5, 1.0, 3.0) after hot deformation at $\alpha+\beta$ region. The results of XRD patterns and selected area electron diffraction indicate that no new phase is identified after adding Ta, although the peaks of both α and β phases shift toward the low angle side with the increase of Ta content. For the Ti-6Al-3Nb-Zr-1Mo-*x*Ta alloy with bimodal structure, the yield strength (YS), ultimate tensile strength (UTS) and microhardness increase due to the increase of molybdenum equivalent ($Mo_{[eq]}$). The influence trend of the Ta content on impact absorb energy is opposite to that on YS, UTS and microhardness. YS, UTS and microhardness are in consistent with the area of shear lip region in the impact fracture surface. When the Ta content is more than 1.0wt%, the corrosion resistance of Ti-6Al-3Nb-2Zr-1Mo-*x*Ta alloys decreases due to the increase of standard balancing potential difference between α and β phases. After potentiodynamic polarization tests, the sample surface area is covered with lots of corrosion pits, which are mainly distributed in the α_p grain interior and α/β interface. Combining YS, impact toughness and corrosion performance, Ti-6Al-3Nb-2Zr-1Mo-1Ta alloy exhibits the optimized compatibility, suggesting its promising potential for marine applications.

Key words: titanium alloy; tantalum; tensile properties; impact toughness; corrosion

Titanium alloys are widely used in the ship and submarine components due to their mass saving and corrosion resistance[1]. Among the Ti alloys, near alpha titanium alloys are usually selected for their weldability and fracture toughness, particularly under the shock conditions, such as the extra-low-interstitial (ELI) Ti-6Al-4V alloy[2,3]. Recently, the Ti-6Al-3Nb-2Zr-1Mo (Ti80) was developed by the Luoyang Ship Material Research Institute as an alternative for Ti-6Al-4V ELI alloy. Ti80 alloy shows a higher fracture toughness with better weldability than ELI Ti-6Al-4V alloy by adjusting alloying elements[4-6]. In addition, the strength of Ti80 is comparable to that of Ti-6Al-4V ELI alloy.

In addition to fracture toughness and weldability, corrosion performance is also considered for marine titanium alloy[7,8]. The corrosion performance of Ti alloys strongly depends on the composition[9-13]. In the biomedical field, large amount of tantalum (Ta) was added in the beta titanium alloys in order to improve the corrosion resistance even though the price is relatively high[14-17]. In addition, Ta as the β-stabilizer element is often added in the near alpha titanium alloys in order to optimize the resistance to seawater corrosion. For instance, Ti-6Al-2Nb-1Ta-0.8Mo alloy is an attractive candidate for modern marine application due to its medium strength, weldability and resistance to seawater corrosion[18].

Received date: March 25, 2020
Foundation item: National Natural Science Foundation of China (51701189, 51775055)
Corresponding author: Wang Qi, Ph. D., Associate Professor, Huanghuai University, Zhumadian 463000, P. R. China, Tel: 0086-396-2824310, E-mail: wagqi609@163.com

It is commonly accepted that adding Ta element in Ti alloys is beneficial for the improvement of corrosion resistance. However, the influence of different Ta contents on corrosion performance of titanium alloys is barely reported, especially taking both corrosion and mechanical properties into consideration. In the present work, the mechanical properties (tensile, microhardness and Charpy impact toughness) and corrosion resistance of Ti-6Al-3Nb-2Zr-1Mo-*x*Ta alloys were investigated in order to optimize the chemical composition of Ti-6Al-3Nb-2Zr-1Mo alloy for the pursuit of excellent corrosion resistance with enhanced mechanical properties.

1 Experiment

The Ti-6Al-3Nb-2Zr-1Mo-*x*Ta (x=0, 0.2, 0.5, 1.0, 3.0, 5.0) alloys were prepared by vacuum consumable electrode arc furnace. The alloy ingots with the mass of 30 kg remelted three times in order to ensure the homogenization of composition. The chemical composition of the casted Ti-6Al-3Nb-2Zr-1Mo-*x*Ta alloys is presented in Table 1. In order to break the coarse as-cast grains, heat forging was firstly carried out at the β phase region, and then performed at the α+β phase region. Finally, the forged Ti-6Al-3Nb-2Zr-1Mo-*x*Ta alloys were annealed at 920 °C for 1 h, and the annealed alloys were used in this investigation. The β transus temperature (T_β) of Ti-6Al-3Nb-2Zr-1Mo-*x*Ta alloys was measured, and their aluminum equivalent ($Al_{[eq]}$) and molybdenum equivalent ($Mo_{[eq]}$) were calculated according to the empirical equation $Al_{[eq]}$=[Al]+0.33[Sn]+0.17[Zr]+10[O] and $Mo_{[eq]}$=[Mo]+0.30[Nb]+0.25[Ta]+0.5[W]+0.72[V]+1.67[Cr]+1.25[Ni]+1.7 [Mn]+1.11[Co]+2.0[Fe][19]. The data are listed in Table 2.

Microstructural characterization was carried out by optical microscope (Leica DMI 5000M) and transmission electron microscope (TEM, JEM-2100). The metallographic specimens were etched by the Kroll's reagent (5 mL HF, 15 mL HNO_3 and 80 mL H_2O) for 15 s. The TEM specimens were prepared by twin-jet electrochemical polisher with the solution of 60vol% methanol, 35vol% butyl alcohol and 5vol% perchloric acid at ~15 V and −20 °C. The phase analysis was performed by X-ray diffraction (XRD, UIV-X) with Cu Kα X-radiation.

The tensile test specimens with diameter of 5 mm and gauge length of 25 mm were prepared and conducted at a strain rate of 5.5×10^{-4} s^{-1} by Instron 5985 testing machine in accordance with the GB/T228.1-2010. The ultimate tensile strength (UTS), yield strength (YS), and elongation to failure (EL) were derived from the average of three repeated tests' results. The microhardness measurement was performed by the HXD-1000TMC/LD hardness tester with a load of 2.94 N for 15 s. The impact absorbed energy of V-shaped notched specimens with cross-section dimensions of 10 mm×10 mm was measured using JB-W300 Charpy impact tester at room temperature in accordance with ASTM E23-16. At least three samples were used for each experimental point.

Electrochemical tests were conducted by the CHI 660B Electrochemical testing system in a conventional three electrode cell, where the saturated calomel electrode was the reference electrode and the Pt wire acted as the counter-electrode. The Ti-6Al-3Nb-2Zr-1Mo-*x*Ta alloys were used as the working electrodes, and the samples with the size of 10 mm×10 mm×2 mm were ground by a series of sandpaper and finally polished to a mirror surface. Electrochemical experiments were performed in 3.5wt%NaCl solution with the analytic grade chemicals and distilled water. The samples were firstly immersed for 1 h and then used for the experiments. The potentiodynamic polarization curves were measured from −2 V to +3 V at a scan rate of 0.01 V/s.

Table 1 Chemical composition of Ti-6Al-3Nb-2Zr-1Mo-*x*Ta alloys (wt%)

x	Al	Nb	Zr	Mo	Ta	C	N	O	H	Ti
0	6.38	3.11	2.00	1.06	0.00	0.033	0.0088	0.084	<0.001	Bal.
0.2	6.38	3.36	2.10	1.19	0.19	0.030	0.0097	0.076	<0.001	Bal.
0.5	6.25	3.41	2.06	1.15	0.53	0.016	0.011	0.093	<0.001	Bal.
1.0	6.37	3.60	1.98	1.20	1.36	0.014	0.012	0.101	<0.001	Bal.
3.0	6.37	3.49	2.06	1.18	2.89	0.019	0.010	0.086	<0.001	Bal.
5.0	6.49	3.76	1.99	1.26	5.32	0.033	0.0092	0.095	<0.001	Bal.

Table 2 β transus temperature (T_β), aluminum equivalent ($Al_{[eq]}$) and molybdenum equivalent ($Mo_{[eq]}$) of Ti-6Al-3Nb-2Zr-1Mo-*x*Ta alloys

x	0	0.2	0.5	1.0	3.0	5.0
T_β/°C	986	982	987	982	978	967
$Al_{[eq]}$	7.56	7.50	7.53	7.72	7.58	7.78
$Mo_{[eq]}$	1.99	2.25	2.31	2.62	2.95	3.72

2 Results and Discussion

2.1 Microstructure and phase composition

The OM images of microstructure of Ti-6Al-3Nb-2Zr-1Mo-*x*Ta alloys are shown in Fig.1. It is clear that when the Ta content is less than 3wt%, a bimodal structure is obtained after hot deformation at the $\alpha+\beta$ region, which is characterized with the equiaxed primary $\alpha(\alpha_p)$ phase and a amount of unglobularized α laths.

The grain size distribution of α_p with its fraction in the Ti-6Al-3Nb-2Zr-1Mo-*x*Ta alloys (*x*=0, 0.2, 0.5, 1.0, 3.0) are shown in Fig.2. It can be found that as the Ta content increases, the average grain size of α_p is 10.5, 13.2, 11.5, 10.3, and 8.5 μm, and the area fraction of α_p are 25.7%, 44.5%, 38.6%, 23.9%, and 31.6%, respectively. For the Ti-6Al-3Nb-2Zr-1Mo-5Ta alloy, a lamellar structure (as seen in Fig.1f) is obtained due to its lowest β transus temperature, as shown in Table 2.

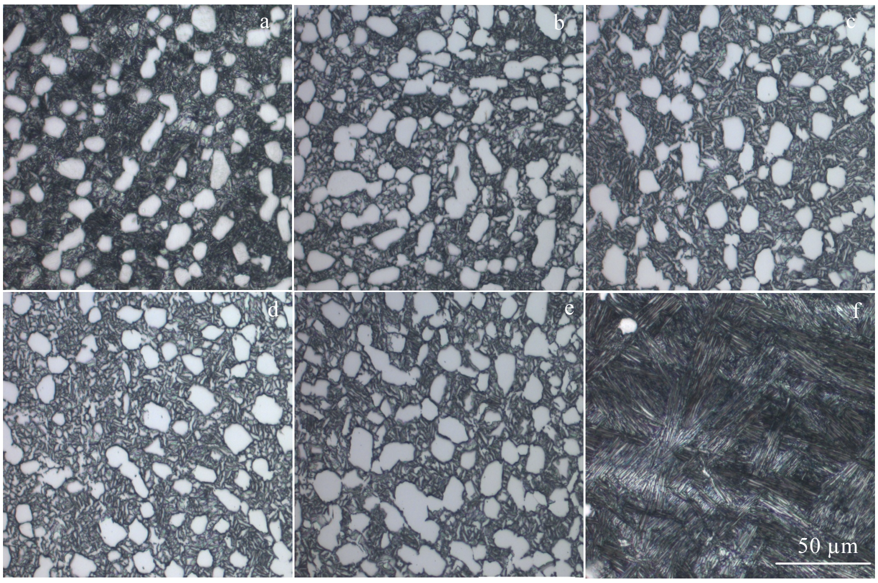

Fig.1 OM images of microstructure of Ti-6Al-3Nb-2Zr-1Mo-*x*Ta alloys: (a) *x*=0, (b) *x*=0.2, (c) *x*=0.5, (d) *x*=1.0, (e) *x*=3.0, and (f) *x*=5.0

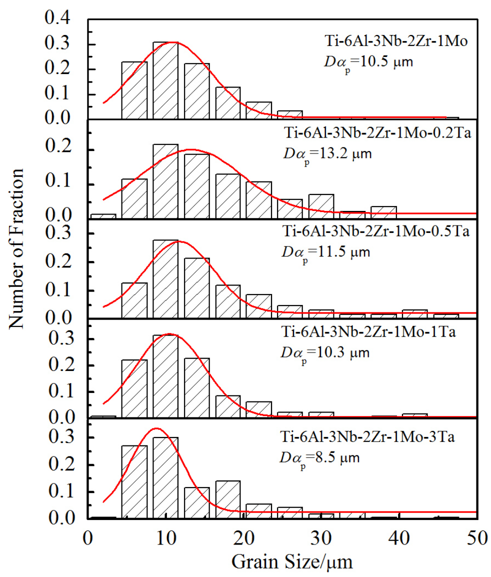

Fig.2 Grain size distribution of α_p in Ti-6Al-3Nb-2Zr-1Mo-*x*Ta (*x*=0, 0.2, 0.5, 1.0, 3.0) alloys

As shown in Fig.3a, the XRD patterns indicate that the Ti-6Al-3Nb-2Zr-1Mo-*x*Ta alloys contain α and β phases, and no new phase is identified after adding Ta into the Ti-6Al-3Nb-2Zr-1Mo alloy, which is also verified by the light field images and selected area electron diffraction results of Ti-6Al-3Nb-2Zr-1Mo and Ti-6Al-3Nb-2Zr-1Mo-5Ta alloy, as shown in Fig.4. However, the XRD peaks of both α and β phases in Ti-6Al-3Nb-2Zr-1Mo shift toward the low angle side after adding Ta element, as shown in Fig.3b. The phenomenon indicates that the lattice parameters of both α and β phases increase as the Ta content increases, which is in consistence with the results of Jiao et al[20].

2.2 Mechanical properties

Fig.5a shows typical stress-strain curves of Ti-6Al-3Nb-2Zr-1Mo-*x*Ta alloys at room temperature. Fig.5b shows the effect of Ta content on the tensile properties of Ti-6Al-3Nb-2Zr-1Mo-*x*Ta alloys. It can be found that the UTS and YS reach the maximum value of 991 and 929 MPa for the Ti-6Al-3Nb-2Zr-1Mo-3Ta alloy. At the same time, its EL is the lowest of 10.2%. It is worth mentioning that after the addition of 0.2wt% Ta, the tensile properties of UTS, YS and EL are simultaneously enhanced.

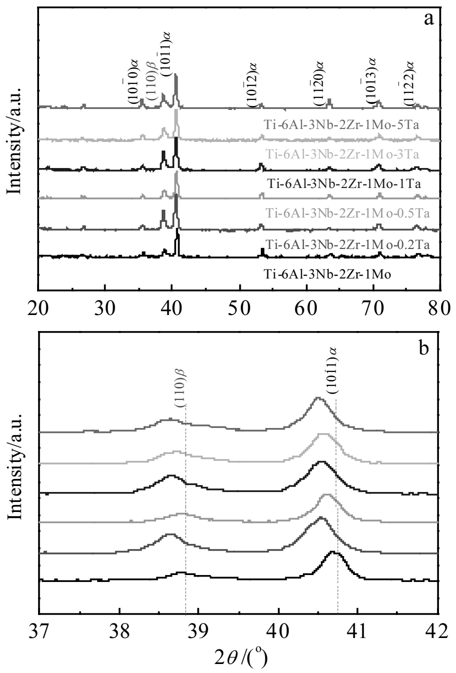

Fig.3 XRD patterns of Ti-6Al-3Nb-2Zr-1Mo-xTa alloys (a); partial enlargement of 37º~42º in Fig.3a (b)

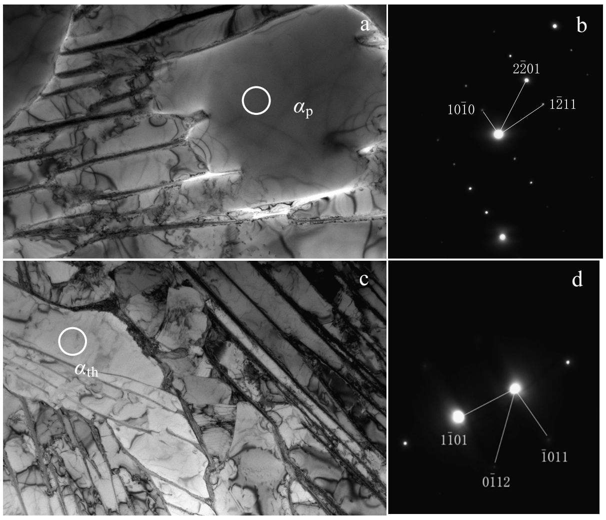

Fig.4 TEM images (a, c) and SAED patterns (b, d) of marked circles for Ti-6Al-3Nb-2Zr-1Mo (a, b) and Ti-6Al-3Nb-2Zr-1Mo-5Ta (c, d) alloys

Influence of Ta content on the microhardness of Ti-6Al-3Nb-2Zr-1Mo-xTa alloys is shown in Fig.6a. The insets are the corresponding OM images of microstructure of alloys after microhardness tests. It can be observed that the variation of microhardness with Ta content is in consistent with variation trend of YS and UTS, as shown in Fig.5b. Deformation configuration of the indentation in Ti-6Al-3Nb-2Zr-1Mo-0.2Ta is shown in Fig.6b. Slip lines caused by dislocation activity can be detected near the edge of indentation, as marked by red arrow in Fig.6b.

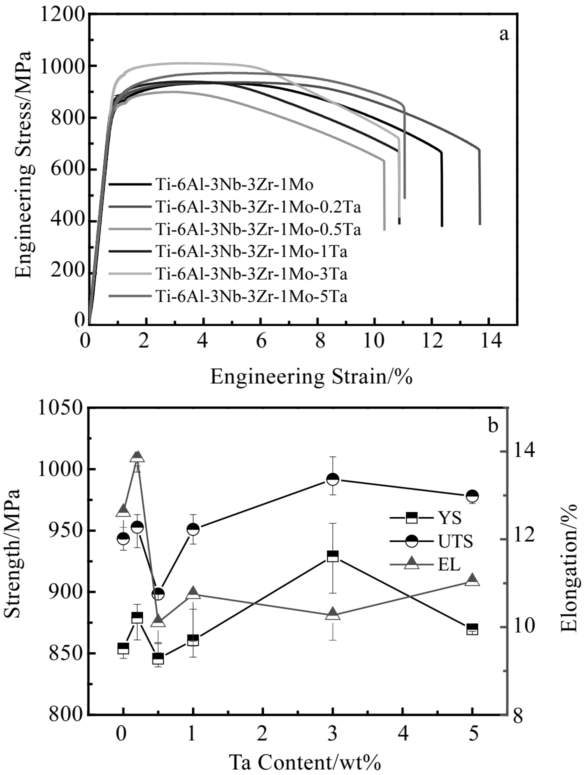

Fig.5 Engineering stress-strain curves (a) and UTS, YS and EL (b) of Ti-6Al-3Nb-2Zr-1Mo-xTa alloys

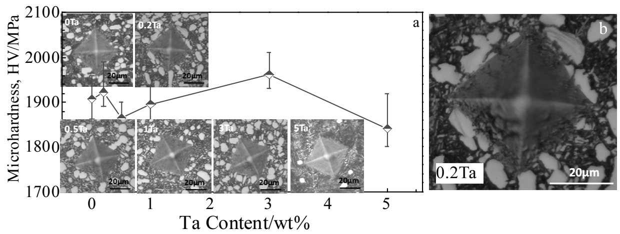

Fig.6 Microhardness and OM images of Ti-6Al-3Nb-2Zr-1Mo-xTa alloys (a) and OM image of Ti-6Al-3Nb-2Zr-1Mo-0.2Ta (b)

Fig.7a displays the influence of Ta content on the impact absorbed energy of Ti-6Al-3Nb-2Zr-1Mo-xTa alloys with the macroscopical impact fracture morphologies. It is clear that the variation trend of impact absorbed energy is opposite to that of YS, UTS and microhardness. The macroscopical fracture is clearly divided into cracking region and shear lip region[21,22], as shown in Fig.7b. With further observation, it can be found that the greater the impact absorbed energy, the larger the shear lip region. For example, the largest area of shear lip region in Ti-6Al-3Nb-2Zr-1Mo-5Ta alloy results in the greatest impact absorbed energy, while the Ti-6Al-3Nb-2Zr-1Mo-3Ta alloy with the smallest area of shear lip region has the least impact absorbed energy.

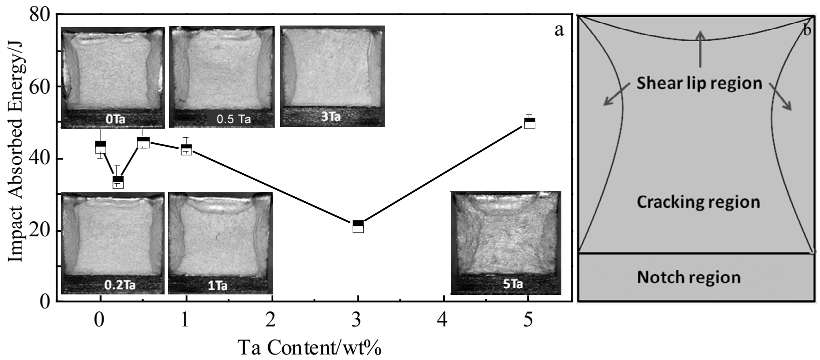

Fig.7 Impact absorbed energy of Ti-6Al-3Nb-2Zr-1Mo-*x*Ta alloys (a); schematic diagram of impact fracture morphology (b)

2.3 Corrosion behavior

Fig.8a shows the typical potentiodynamic polarization curves of Ti-6Al-3Nb-2Zr-1Mo-*x*Ta alloys in 3.5wt% NaCl solution. It displays that as the potential increases, the current density firstly increases rapidly due to activation polarization, and then increases slowly due to the passivation behavior. Finally, the current density of all the alloys is suppressed and remains at a particular level with increasing the potential over 0 V vs. SCE, which can be attributed to the occurrence of pitting corrosion[23].

The corrosion potential (E_{corr}) and the corrosion current density (I_{corr}) of Ti-6Al-3Nb-2Zr-1Mo-*x*Ta alloys obtained from the polarization curves through Tafel extrapolation method are shown in Fig.8b. In general, the higher value of E_{corr} causes more difficulties to corrode, and the smaller value of I_{corr} causes lower corrosion rate of the alloy once the corrosion occurs[24-26]. In Fig.8b, the value of I_{corr} and E_{corr} in the Ti-6Al-3Nb-2Zr-1Mo-0.5Ta alloy is minimum, which indicates that the corrosion rate of Ti-6Al-3Nb-2Zr-1Mo-0.5Ta alloy is the lowest, although it is prone to corrode. After comprehensive comparison, it is found that the Ti-6Al-3Nb-2Zr-1Mo-1Ta alloy shows the best corrosion resistance and the corrosion rate is also relatively low, i.e., the comprehensive corrosion performance is better than other alloys.

The microstructures of Ti-6Al-3Nb-2Zr-1Mo-*x*Ta alloys after potentiodynamic polarization experiments are shown in Fig.9. Compared with the microstructures before potentiodynamic polarization experiments (Fig.1), the sample surface are covered with lots of corrosion pits. After close observation, it can found that these corrosion pits are mainly distributed in the α/β interface and α_p grain interior. In general, the generation of corrosion pits results from the dissolution of protective oxide films (mainly TiO_2). Thus, the results suggest that α/β interphase boundary and α_p serve on the preferential dissolution location, which is in consistent with the results of previous studies[27-29].

The above results suggest that the effect of Ta content on the properties of Ti-6Al-3Nb-2Zr-1Mo-*x*Ta alloys is complex. Combining yield strength, impact toughness and corrosion performance, Ti-6Al-3Nb-2Zr-1Mo-1Ta alloy exhibits the best compatibility, as shown in Fig.10. In addition, the variation of yield strength with Ta content is opposite to that of impact toughness. When Ta content is less than 3wt%, the microstructural characteristics of Ti-6Al-3Nb-2Zr-1Mo-*x*Ta alloys are similar, as shown in Fig.1a~1e. In this case, their yield strength and impact toughness are not sensitive to the microstructure, but mainly depend on the molybdenum equivalent ($Mo_{[eq]}$). As shown in Table 2, the $Mo_{[eq]}$ gradually increases with the increase of Ta content, which results in the overall increase of yield strength and decrease of impact absorbed energy. For Ti-6Al-3Nr-2Zr-1Mo-5Ta alloy, its yield strength decreases and impact absorbed energy increases because its microstructure is in better consistent with the characteristics

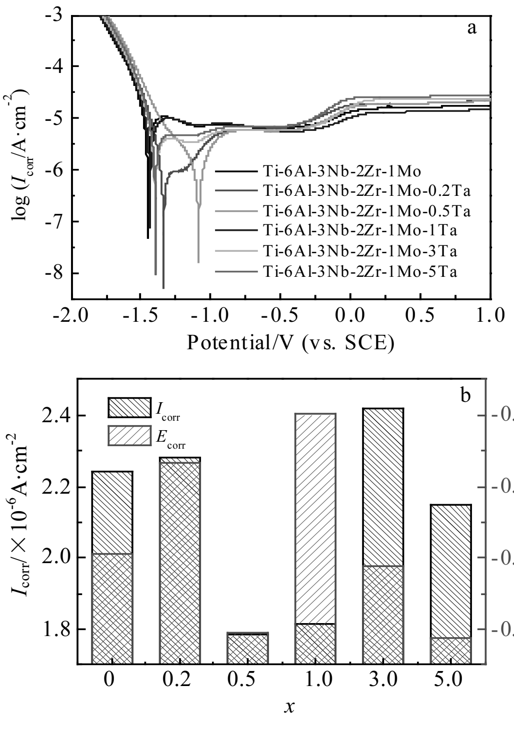

Fig.8 Potentiodynamic polarization curves in 3.5wt% NaCl solution(a); corrosion potential and corrosion current density of Ti-6Al-3Nb-2Zr-1Mo-*x*Ta alloys (b)

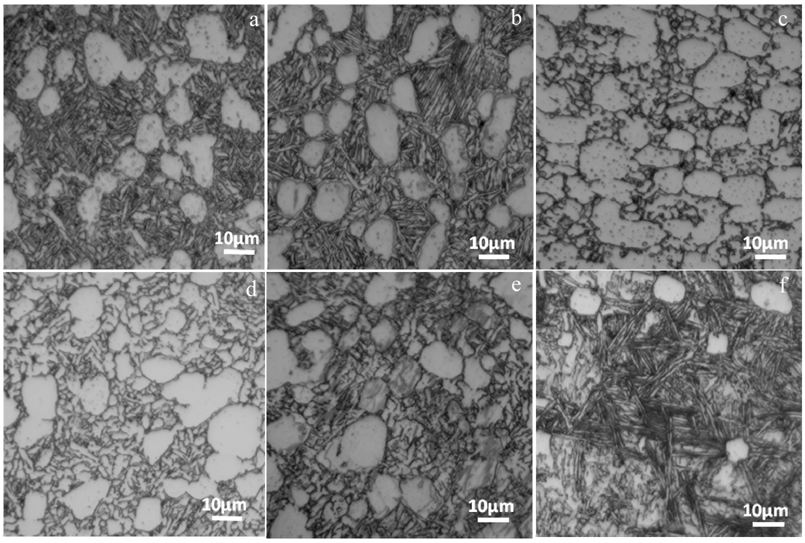

Fig.9 OM images of microstructure of Ti-6Al-3Nb-2Zr-1Mo-xTa alloys after potentiodynamic polarization experiments: (a) x=0, (b) x=0.2, (c) x=0.5, (d) x=1.0, (e) x=3.0, and (f) x=5.0

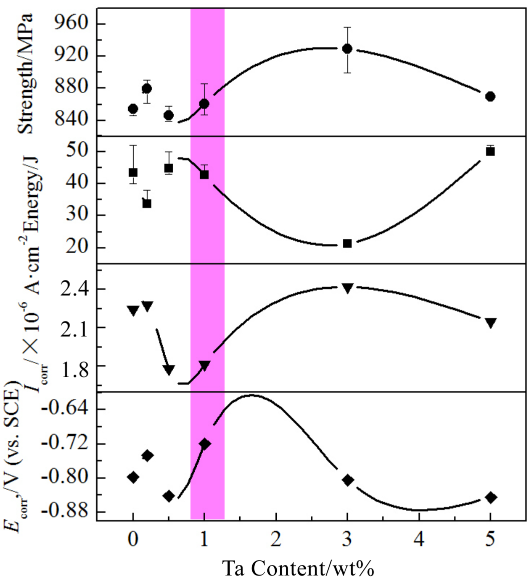

Fig.10 Yield strength, impact toughness and corrosion performance of Ti-6Al-3Nb-2Zr-1Mo-xTa alloys

of lamellar structure. The pitting corrosion results from the formation of micro-galvanic cells due to the standard balancing potential difference between α and β phase, which is sensitive to the difference in the composition of α and β phases[30]. With the increase of Ta content, the corrosion resistance of Ti-6Al-3Nb-2Zr-1Mo-xTa alloys decreases because the standard balancing potential difference between α and β phases increases.

3 Conclusions

1) For Ti-6Al-3Nb-2Zr-1Mo-xTa alloys (x=0, 0.2, 0.5, 1.0 and 3.0), a bimodal structure is obtained after hot deformation in the $\alpha+\beta$ region. However, a lamellar structure is obtained in Ti-6Al-3Nb-2Zr-1Mo-5Ta due to its lowest β transus temperature, T_β.

2) When the Ta content is less than 5wt%, no new phase is identified in the Ti-6Al-3Nb-2Zr-1Mo-xTa alloys. However, the XRD peaks of both α and β phases shift toward the low angle side with the increase of Ta content.

3) In general, except for the lamellar structure in Ti-6Al-3Nb-Zr-1Mo-5Ta alloy, the YS, UTS and microhardness increase due to the increase of molybdenum equivalent $Mo_{[eq]}$ in Ti-6Al-3Nb-2Zr-1Mo-xTa alloys.

4) The variation trend of impact absorbed energy with different Ta contents is opposite to that of YS, UTS and microhardness, and is in consistent with the area of shear lip region. Ti-6Al-3Nb-2Zr-1Mo-5Ta alloy exhibits the highest impact absorbed energy due to its lamellar microstructure.

5) The corrosion performance of Ti-6Al-3Nb-2Zr-1Mo-1Ta alloy is the best due to its lower corrosion current density I_{corr} and higher corrosion potential E_{corr}. After potentiodynamic polarization test, the sample surfaces are covered with lots of corrosion pits, which are mainly distributed in the α/β interface and α_p grain interior, due to the standard balancing potential difference between α and β phases.

References

1 Chen J, Wang T X, Zhou W *et al*. *Titanium*[J], 2015, 32: 8
2 Banerjeea D. *Acta Mater*[J], 2013, 61: 844
3 Gurrappa I. *Materials Characterization*[J], 2003, 51(2-3): 131
4 Guo K, Meng K, Miao D. *Materials Science and Engineering A*[J], 2019, 766 (24): 138 346

5 Wang Q, Ren J Q, Wu Y K *et al. Journal of Alloys and Compounds*[J], 2019, 789 (15): 249
6 Xiong J H, Li S K, Gao F Y *et al. Materials Science and Engineering A*[J], 2015, 640 (29): 419
7 Atapour M, Pilchak A L, Shamanian M *et al. Materials & Design* [J], 2011, 32 (3): 1692
8 Chuvil'deev V N, Kopylov V I, Berendeev N N *et al. Journal of Alloys and Compounds*[J], 2019, 790 (25): 347
9 Yan S K, Song G L, Li Z X *et al. Journal of Materials Science & Technology*[J], 2018, 34 (3): 421
10 Jiang Z L, Dai X, Middleton H. *Materials Science and Engineering B*[J], 2011, 176: 79
11 Yu S Y, Brodrick C W, Ryan M P *et al. J Electrochem Soc*[J], 1999, 146: 4429
12 Xia C Q, Zhang Z G, Feng Z H *et al. Corrosion Science*[J], 2016, 112: 687
13 Lu J W, ZhaoY Q, Niu H Z *et al. Materials Science and Engineering C*[J], 2016, 62 (1): 36
14 Lucia C T, Daniel M, Carmen S. *Materials Chemistry and Physics*[J], 2020, 240 (15): 122 229
15 Zhou Y L, Mitsuo N, Toshikazu A *et al. Materials Science and Engineering A*[J], 2005, 398: 28
16 Karen A S, Alain R. *Materials Chemistry and Physics*[J], 2007, 103 (2-3): 351
17 Zhou Y L, Niinomi M, Akahori T. *Materials Science and Engineering A*[J], 2004, 371: (1-2): 283
18 Miller W H, Chen R T, Starke E A. *Metallurgical Transactions A* [J], 1987, 18 (8): 1451
19 Lütjering G, Williams J C. *Engineering Materials Processes*[M]. Berlin, Heidelberg: Springer, 2010
20 Mi K H, Moon J H, Min S Y *et al. Materials Science and Engineering A*[J], 2014, 616 (20): 268
21 Nikolas H, Ryan W, Enrico L. *Materials Science and Engineering A*[J], 2019, 742 (10): 269
22 Buirette C, Huez J, Gey N *et al. Materials Science and Engineering A*[J], 2014, 618 (17): 546
23 Zhou Y L, Luo D M. *Journal of Alloys and Compounds*[J], 2011, 509 (21): 6267
24 Liu R, Cui Y, Liu L *et al. Corrosion Science* [J], 2019, 19: 108 402
25 Shamir M, Junaid M, Khan F N *et al. Journal of Materials Research and Technology*[J], 2019, 8 (1): 87
26 Li Q, Li J, Ma G H *et al. Materials & Design*[J], 2016, 111 (5): 421
27 Yang Y, Xia C, Feng Z *et al. Corrosion Science*[J], 2015, 101: 56
28 Lu J W, Ge P, Li Q *et al. Journal of Alloys and Compounds*[J], 2017, 727: 1126
29 Chuvil'deev V N, Kopylov V I, Nokhrin A V *et al. Journal of Alloys and Compounds* [J], 2019, 785 (15): 1233

Ta 含量对 Ti-6Al-3Nb-2Zr-1Mo-*x*Ta 合金力学性能和腐蚀性能的影响

王 启[1,3]，任军强[2]，张斌斌[3]，吴宇坤[3]，叶 苗[1]，邵 珊[2]
(1. 黄淮学院，河南 驻马店 463000)
(2. 兰州理工大学 省部共建有色金属先进加工与再利用国家重点实验室 材料科学与工程学院，甘肃 兰州 730050)
(3. 洛阳船舶材料研究所，河南 洛阳 471039)

摘 要：系统研究了 Ti-6Al-3Nb-2Zr-1Mo-*x*Ta (*x*=0, 0.2, 0.5, 1.0, 3.0, 5.0)合金的微观组织、拉伸性能、夏比冲击韧性和耐海水腐蚀性。结果表明，经 $\alpha+\beta$ 两相区锻造后，Ti-6Al-3Nb-2Zr-1Mo-5Ta 合金获得片层组织，Ti-6Al-3Nb-2Zr-1Mo-*x*Ta (*x*=0, 0.2, 0.5, 1.0, 3.0)均获得双态组织。XRD、TEM 和选区电子衍射表明，在添加 Ta 元素后，Ti-6Al-3Nb-2Zr-1Mo-*x*Ta 合金没有新相产生。对于双态组织 Ti-6Al-3Nb-Zr-1M0-*x*Ta 合金，随着 Ta 含量的增加，其 Mo 当量逐渐增加，导致其屈服强度、抗拉强度和显微硬度均有所提高。而 Ta 含量对冲击吸收功的影响规律与屈服强度和抗拉强度的影响规律相反，其大小与冲击断口剪切唇区面积一致。当 Ta 含量超过 1.0%(质量分数)时，由于 α 和 β 相之间的标准平衡电位差逐渐增大，Ti-6Al-3Nb-2Zr-1Mo-*x*Ta 合金的耐海水腐蚀逐渐降低。综合考虑强度、冲击韧性和耐海水腐蚀性能，Ti-6Al-3Nb-2Zr-1Mo-1Ta 合金综合匹配性最好，具有良好的海洋工程应用潜力。
关键词：钛合金；钽；拉伸性能；冲击韧性；腐蚀

作者简介：王 启，男，1985 年生，博士，副教授，黄淮学院机械与能源工程学院，河南 驻马店 463000，电话：0396-2824310，E-mail: wangqi609@163.com